A Bayesian Approach to Subkilometer Crater Shape Analysis Using Individual HiRISE Images

Rodrigo Savage, Leon F. Palafox, Clayton T. Morrison, Jeffrey J. Rodriguez, *Senior Member, IEEE*, Kobus Barnard, *Member, IEEE*, Shane Byrne, and Christopher W. Hamilton

***Abstract*— The ages of terrains on other planetary bodies are chiefly determined using crater size–frequency distributions. However, primary impacts can generate numerous secondary craters that can affect the crater population. Classifying impact craters as primary or secondary is commonly done via time-consuming manual inspection, which limits the areas that can be analyzed at high resolution. We present a parametric model for characterizing small (100–600 m diameter) impact craters, where the model parameters have implications for describing the physical processes involved in their formation and modification. We infer these parameters from craters in images captured by the high-resolution imaging science experiment (HiRISE) camera onboard the Mars Reconnaissance Orbiter. For each crater within the appropriate size range, our algorithm creates a 3-D surface for a parametrically modeled crater and a 2-D rendering using illumination metadata, including emission, phase, and solar incidence angles at the time when the image was captured. A function describes the likelihood of each set of model parameters in terms of the geometry of craters in a given HiRISE image. These values are then optimized using a Metropolis–Hasting Markov chain Monte Carlo sampler. We evaluated three different prior probability distributions over the parameter space and two different likelihoods: one for digital terrain models and the other for images. We show that after applying t-distributed stochastic neighbor embedding (t-SNE) over the inferred crater parameters, t-SNE is able to project the multidimensional crater parameters into a 2-D space where secondary craters cluster together and are separable from primary craters.**

***Index Terms*— Image analysis, image generation, image shape analysis, rendering (computer graphics).**

I. Introduction

PLANETARY surfaces such as those on Mars have complex geologic histories that are modified by impact cratering, volcanism, tectonics, fluvial, aeolian, glacial, and periglacial processes. These geological processes provide insight into how the Martian surface has changed through time, as well as where and when environments on Mars may have sustained liquid water. The size–frequency distributions of impact crater populations are used to date planetary surfaces and constrain resurfacing rates [1]. In general, higher crater number densities imply older surface ages or slower crater removal processes. Crater morphology also provides insight into target material properties [2], including the distribution of subsurface volatiles [3], [4], variations in the strength of geologic material [5], and surface modification processes [6], [7].

The size–frequency distribution of craters can be approximated by a power law [1], [8], where larger craters are rare and smaller craters are more abundant. Age is related to the density of crater number and their size. On the Moon, absolute age is independently known for a limited number of locations through the analysis of samples returned by the Apollo missions [9]. These ages are compared to observed crater size–frequency distributions to infer the impactor flux striking the Moon through time [10]. Orbital dynamic models and scaling relationships are then used to estimate the impactor flux, impactor type, velocity, and expected crater size–frequency distributions in other parts of the Solar System [1]. Isochron diagrams can then be used to relate observed crater populations to absolute model ages [1], and these relationships can be directly evaluated using remote-sensing observations of current impact cratering rates [11].

Extrapolation of lunar-calibrated models to Mars carries large systematic uncertainties that affect the model ages of Martian surfaces [1]. Additionally, statistical uncertainty in the observed crater population can introduce random errors. These random errors can be estimated using Poisson statistics, such that the random uncertainty scales with the square root of the crater number density [11]. Accurate dating of surfaces thus requires measuring large numbers of craters. However, terrains that are young, or geographically small, may not include enough large craters to sufficiently reduce the influence of random errors. Therefore, crater counts may need to be extended to include small craters, which increase the risk of the population being contaminated by secondaries. Using impact craters to date planetary surfaces requires two fundamental assumptions: the impact cratering rate must be known through time, and the craters must be spatially random. Secondary craters violate both of these assumptions.

Secondary craters form when debris from a primary crater impacts the surface elsewhere, creating new craters [12]. On Mars, secondary crater diameters are typically less than 5% of their associated primary crater's diameter [13] and can

Manuscript received June 28, 2017; revised November 25, 2017; accepted December 19, 2017. Date of publication May 11, 2018; date of current version September 25, 2018. This work was supported in part by the Consejo Nacional de Ciencia y Tecnologia and in part by the NASA Mars Data Analysis Program under Grant NNX14AN77G. *(Corresponding author: Rodrigo Savage.)*

R. Savage and J. J. Rodriguez are with the Department of Electrical and Computer Engineering, The University of Arizona, Tucson, AZ 85721 USA (e-mail: rodrigosavage@email.arizona.edu).

L. F. Palafox, S. Byrne, and C. W. Hamilton are with the Lunar and Planetary Laboratory, The University of Arizona, Tucson, AZ 85721 USA.

C. T. Morrison is with the School of Information, The University of Arizona, Tucson, AZ 85721 USA.

K. Barnard is with the Department of Computer Science, The University of Arizona, Tucson, AZ 85721 USA.

Digital Object Identifier 10.1109/TGRS.2018.2825608

be an important component of an impact crater population at small crater sizes [13]. However, secondary craters form at an unsteady rate at clustered locations. For instance, Zunil Crater—located in the Cerberus Plains region of Mars—generated approximately 10^7 secondary craters, ranging 10–200 m in diameter [13], which are concentrated in the surrounding area and formed almost simultaneously.

Debris ejected from a parent crater that lands nearby the parent may impact with a low velocity, generating small, shallow, and irregularly shaped craters; however, distant secondary craters may be generated by debris traveling at higher velocities and have morphologies resembling primary craters [14]. Distant (high-velocity) secondaries cannot be easily separated from the primary crater population, even by trained geologists. However, geologists can recognize most low-velocity secondary craters through several criteria: they are shallower than primaries of the same diameter, they may have irregularly shaped rims, and they may be arranged in clusters or rays emanating from the primary impact site [14].

To date, most crater classification has been conducted by labor-intensive manual inspection. While automated crater detection algorithms (CDA) exist [15]–[21], they are not able to reliably distinguish between primary and secondary craters, and they count all craters as primary.

We present a new method to characterize impact crater morphologies and distinguish between primary and secondary craters using satellite imagery. We represent craters with a parametric model defined by crater diameter, rim height, rim eccentricity and orientation, angle of repose, and depth of sedimentary infill. To infer the parameters that characterize the crater, we take a Bayesian approach, which treats these parameters as random variables (a random variable maps the outcome of a random phenomenon to a number). A prior distribution model expresses our prior knowledge about the probability of various values of these unknown crater parameters. We define three prior parameter distributions: one describing primary craters, another describing secondary craters, and a uniform prior to assess the primary and secondary priors. The primary and secondary priors are based on the differences between primary and secondary craters' shape, size, and depth-to-height ratio [14], [22], [23]. We formulated two different functions to assess the likelihood of the input data, depending on the type of the data source: one for the grayscale images acquired by the high-resolution imaging science experiment (HiRISE) [24], onboard the Mars Reconnaissance Orbiter (MRO), and stereoderived digital terrain models (DTMs) generated from HiRISE imagery [25]. A DTM is a 2-D array of elevation measurements representing the height of the terrain. The grayscale image likelihood function computes the probability density of the image pixels. Similarly, the DTM likelihood function computes the probability density for the crater's surface shape. To derive the posterior probability distribution for the crater model parameters, we use Bayes' formula to revise our prior knowledge

$$p(X|I) \propto p(I|X)p(X) \tag{1}$$

where X is a vector representing the crater parameters, $p(X)$ is the joint probability distribution from any of the three prior distributions, and $p(I|X)$ is the likelihood for the data, I, defined separately for grayscale and DTM data. The posterior distribution $p(X|I)$ cannot be optimized analytically in closed form, so we develop a Metropolis–Hastings (MH) Markov chain Monte Carlo (MCMC) sampler to estimate the parameters that maximize the posterior, that is, the parameters for a crater morphology that appear to best explain the image or DTM data under the given prior. Finally, we evaluate how well this modeling approach distinguishes primary from secondary craters by assessing how the parameters that maximize the posterior probability cluster depending on the type of crater. The parameters are high dimensional, so we project them into a 2-D space using t-distributed stochastic neighbor embedding (t-SNE) [26]. We find that the projection forms linearly separable clusters distinguishing primary from secondary craters. This paper offers several novel contributions: 1) we demonstrate that a single image can be used to automatically and reliably model crater shapes; 2) we show that the search over the parameter space can be guided by using prior distributions informed by empirical analysis of crater morphologies; and 3) we show that the inferred crater parameters can be used to separate primary craters from secondary craters in a small test set of images.

II. Related Work

Jahn [15] was one of the first to implement a CDA for Mars. Jahn [15] applied the Hough transform to edge maps obtained by Canny edge detection applied to grayscale images from the Viking orbiters. Jahn [15] achieved good results with synthetic images but poor results with Viking images because of the high number of false positives in the classification.

In 1999, improvements to the circular Hough transform made it more resilient to noise, scale, and illumination variations [27], leading to a variety of new algorithms for automated landform detection, including the identification of impact craters [16], [28], [29]. For example, in the context of impact crater detection on Mars, Kim *et al.* [16] improved upon the modified Hough transform method by constructing an algorithm that included three stages: "focusing" to identify regions of interest within an image, "organization" using conic section fitting to identify impact craters, and "refinement and verification" using template matching combined with the application of a neural network to remove false positives. The algorithm achieved an accuracy between 70% and 90% and a quality factor between 60% and 80%, where accuracy is defined as $\mathrm{TP}/(\mathrm{TP}+\mathrm{FN})$ and quality factor as $\mathrm{TP}/(\mathrm{TP}+\mathrm{FN}+\mathrm{FP})$, where TP is the number of true positives (craters detected by the algorithm that are in the location of a real crater), FN is the number of false negatives (craters not detected by the algorithm), and FP is the number of false positives (features detected by the algorithm that are not craters).

In an alternative approach to impact crater detection, Bandeira *et al.* [18] used a method involving three steps: "candidate selection" using image thresholding to enhance shadows produced by the raised crater rim morphology and reduce noise, "template matching" using a fast Fourier transform (FFT) to develop correlations between the binary image

TABLE I
CRATER LOCATIONS DEFINED USING THE "MARS 2000" PROJECTION

Crater	Latitude	Longitude	DTM	Grayscale Image
$crater_1$	$173.026°E$	$27.915°N$	DTEEC_026461_2080_026738_2080_A01	ESP_026461_2080_RED_C_01_ORTHO
$crater_2$	$131.911°E$	$15.065°S$	DTEEC_037948_1645_038291_1645_A01	ESP_037948_1645_RED_C_01_ORTHO
$crater_3$	$131.887°E$	$14.953°S$	DTEEC_037948_1645_038291_1645_A01	ESP_037948_1645_RED_C_01_ORTHO
$crater_4$	$169.675°E$	$9.560°N$	DTEED_025459_1895_026514_1895_A01	ESP_037948_1645_RED_C_01_ORTHO
$crater_5$	$169.666°E$	$9.565°N$	DTEED_025459_1895_026514_1895_A01	ESP_037948_1645_RED_C_01_ORTHO
$crater_6$	$169.658°E$	$9.567°N$	DTEED_025459_1895_026514_1895_A01	ESP_037948_1645_RED_C_01_ORTHO

scenes as a series of impact crater templates, and "crater detection" using an analysis of the probability volume generated by the FFT to identify the most likely locations and dimensions of impact craters within the scene. The resulting classifier had a true positive rate of 86.57% and a false positive rate of 15.95%.

Urbach and Stepinski [17] developed a more robust algorithm that uses techniques from facial recognition, such as Hu's seven moments of invariance [30] and morphological operations [31] to detect subkilometer craters. Urbach and Stepinski [17] assumed that craters always appear in the image as a pair of crescent-like highlight and shadow regions. They defined the highlight image as the input image and the shadow image as the negative input image. For the highlight and shadow images, they performed background removal followed by a power and area filter using morphological closing operations. They applied a shape filter, using Hu's moments, matched shadow regions with highlighted regions to create a crater candidate list, and then trained a decision tree to identify craters. They reported that in some cases, the false negatives exceeded the number of true positives. Consequently, more recent research has targeted improvement of the machine learning step that classifies craters [19], [32].

Martins *et al.* [33] hypothesized that craters are similar to human faces in the sense that they have many regional features. Martins *et al.* [33] used several weak classifiers, each having a simple threshold on a single image feature, which were combined in an iterative procedure to create a strong classifier. Martins *et al.* [33] argued that they are able to detect craters that have a diameter of seven pixels or greater.

Ding *et al.* [34], using the framework from [17] and insights from [33], created a classifier to distinguish between craters and noncraters. Ding *et al.* [34] extended the prior research by using a least absolute shrinkage and selection operator and a Bayesian classifier with an L1 regularizer [20] to classify craters with features from the Urbach and Stepinski [17] step. Later, one of Ding's students, Cohen *et al.* [21] proposed crater detection via convolutional neural networks. Wang *et al.* [35] implemented Urbach and Stepinski's [17] pipeline and modified the classification stage with sparse boosting and a reduced set density estimator. Even though Wang *et al.* [35] achieved an 85% accuracy (compared to 89% by Cohen *et al.* [21]), the stated contribution was being able to detect craters fast enough for automated descent and landing of planetary probes.

III. TEST DATA

To evaluate our modeling approach, we used MRO HiRISE images [24] and stereoderived DTMs [25]. We chose three DTMs: 1) DTEEC_026461_2080_026737_2028_A01, which contains one primary crater greater than 600 m in diameter, named $crater_1$; 2) DTEEC_037948_1645_038291_1645_A01, which includes two primary craters greater than 400 m in diameter, with the northern crater named $crater_2$ and southern crater named $crater_3$; and 3) DTEED_025459_1895_026514_1895_A01, which contains clusters of secondary craters (most likely sourced from Zunil Crater), named $crater_4$, $crater_5$, and $crater_6$. Each of these DTMs also includes an orthorectified stereopair of images. Image identification numbers and coordinate locations for each crater are shown in Table I, and all original data are available through the NASA Planetary Data System (https://pds.nasa.gov). Although DTMs are not necessary for inferring craters using our image grayscale likelihood, we used the DTMs as a baseline for assessing the crater shapes developed by our algorithm.

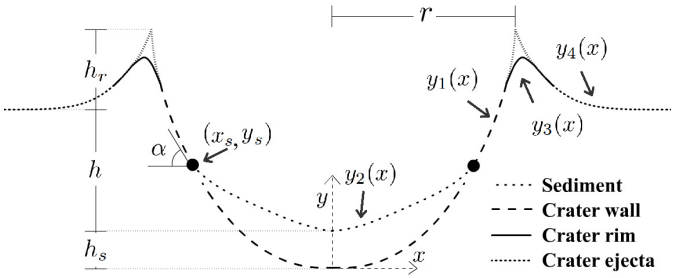

Fig. 1. Crater parametric model is formed by four curves stitched together, which are labeled as y_1, y_2, y_3, and y_4. The crater center is located at the bottom of the crater and serves as the origin for the x and y coordinates relative to the crater center; x increases outward from the center and y increases upward. This view shows the major-axis cross section, where the crater radius is r.

IV. PARAMETRIC MODEL

A. Overview of the Parametric Model

We define a parametric crater surface with nine random variables: center latitude and longitude; the crater rim is defined by an elliptical shape, which is described by its semimajor axis length, r, semiminor axis length, r_{minor}, and the angle of rotation for the ellipse, ϕ; height of the sedimentary infill within the crater, h_s; angle of repose of the sediment, α; height of the crater rim, h_r; and crater depth, h. These parameters combine to form a crater with the geometry shown in Fig. 1, where the composite crater profile curve, $y(x)$, is formed by seamlessly stitching together four curves, as shown in

$$y(x) = \begin{cases} y_1(x) & 0 \leq x \leq x_s \\ y_2(x) & x_s < x \leq r - \frac{r}{12} \\ y_3(x) & r - \frac{r}{12} < x \leq r + \frac{r}{12} \\ y_4(x) & r + \frac{r}{12} < x \leq 2r. \end{cases} \tag{2}$$

Fig. 1 and (2) apply to points lying along the major axis of the crater.

The 3-D surface of the crater model is constructed by rotating the profile in Fig. 1 around the center axis, scaling parametric curve in (2) by the radius r according to the boundary of the crater rim ellipse. For other crater points, the independent variable x is computed as a scaled version of the radial distance, ρ, from the crater center. Let (ρ, θ) be the polar coordinates of an arbitrary point within the crater. The crater radius at angle θ is given by the well-known equation

$$r_\theta = \frac{r\, r_{\text{minor}}}{\sqrt{[r_{\text{minor}} \cos(\theta - \phi)]^2 + [r \sin(\theta - \phi)]^2}}. \tag{3}$$

For point (ρ, θ) within the crater, we compute x by scaling ρ according to the crater radius at angle θ

$$x(\rho, \theta) = \rho r / r_\theta. \tag{4}$$

Thus, we obtain

$$x(\rho, \theta) = \rho \frac{\sqrt{[r_m \cos(\theta - \phi)]^2 + \sin(\theta - \phi)^2}}{r_m}. \tag{5}$$

To simplify the derivation of parametric curves for use in (2), we normalize all craters so that the semimajor axis length is 1; the semiminor axis length is scaled accordingly to be r_m.

A fresh secondary crater could be shallow and still have a well-preserved rim; this is modeled by relatively large values of h_s, α, and h_r. On the other hand, an old primary crater might exhibit a rim that has slumped into the interior of the crater, thus also having larger h_s and α but smaller h_r. Craters are not necessarily rotationally symmetric, and secondary craters tend to be elliptical [14]. Because our goal is to differentiate between primary and secondary craters, it is important to have parameters that model the eccentricity of a crater.

B. Parametric Curves

Curve y_1 describes sediment that has accumulated over time on the crater floor. This sediment can be rim material falling into the crater, or aeolian sediment settling into the crater. Curve y_1 is defined as a third-order polynomial

$$y_1 = h_s + c_2 x^2 + d_2 x^3. \tag{6}$$

The constants c_2 and d_2 were found by solving a system of equations representing the following constraints: 1) curve y_1 passes through (x_s, y_s) and 2) at the point (x_s, y_s), the slope of curve y_2 equals the tangent of the angle of repose.

Curve y_2 describes the shape of a fresh bowl-shaped impact crater [36], and it is defined as a quadratic function

$$y_2 = (h + h_s + h_r)\left(\tfrac{x}{r}\right)^2 \tag{7}$$

where h is the crater depth measured from ground level to the lowest point of the crater, h_s is the depth of the sedimentary infill within the crater, and h_r is the height of the crater rim measured from ground level to the highest point of the rim. The crater depth is constrained by the semimajor axis, r, where $h = 0.1624(2r) + 0.0065$ [23].

The angle of repose α describes the maximum surface slope angle for which a granular material is stable; if the surface angle inclines beyond this point, additional sediment will slide down and accumulate at the bottom of the crater. The point (x_s, y_s), where the slope of y_2 equals the tangent of the angle of repose, is given by the following equation:

$$x_s = \frac{\tan(\alpha) r^2}{2(h + h_s + h_r)}. \tag{8}$$

Curve y_3 describes the shape of the crater rim and is defined as a third-order polynomial

$$y_3 = y_s + b_3 x + c_3 x^2 + d_3 x^3. \tag{9}$$

We empirically sampled 30 small craters in the DTMs and determined that the shape was adequately fit by a third-order polynomial. The constants b_3, c_3, and d_3 are found by solving a system of equations to ensure that the slope of the curve matches the slopes of the adjacent curve segments.

Curve y_4 describes the crater ejecta and uplifted terrain outside the crater rim [36] and is defined by

$$y_4 = h_r \left(\frac{r}{x}\right)^3 + h + h_s. \tag{10}$$

Curve y_4 connects with y_3 and projects to a rim crest that would meet the projection of y_1 at the point $(r, h_s + h + h_r)$. However, to realistically model the crater rim, the projected rim crest is replaced by curve y_3. Curve y_4 also follows the decay described in [36]. In our implementation, we extend curve y_4 outward to a distance of twice the crater radius $(2r)$ from the crater center. To fit craters on a slope, plane rotation is removed by detrending the surface [37].

C. DTM Likelihood

The likelihood of the DTM data given the model parameters is approximated as being proportional to e^{-E_d}, where E_d is the mean squared error between our parametric crater model and the relevant portion of the corresponding HiRISE DTM

$$E_d = \frac{\sum_i C(x_i, y_i)[\text{dtm}(x_i, y_i) - y(\rho, \theta)]^2}{\sum_i C(x_i, y_i)}. \tag{11}$$

The function $\text{dtm}(x_i, y_i)$ returns the height value of the DTM at point (x_i, y_i), and $y(\rho, \theta)$ is the height of the parametric crater evaluated at polar coordinates (ρ, θ). Let (x_c, y_c) be the center of the parametric crater. The values of ρ and θ are computed from the crater-relative rectangular coordinates as follows:

$$\rho = \|(x_i, y_i) - (x_c, y_c)\| \tag{12}$$

$$\theta = \arctan\left(\frac{y_i - y_c}{x_i - x_c}\right). \tag{13}$$

Let $C(x_i, y_i)$ be an indicator variable defined as 1 in regions where the parametric model is a crater, and 0 otherwise.

D. Grayscale Likelihood

The likelihood of the grayscale HiRISE image data given the model parameters is approximated as being proportional to e^{-E_i}, where E_i is the mean squared error between our 2-D rendering of the parametric crater model and the corresponding portion of the HiRISE image

$$E_i = \frac{\sum_i C(x_i, y_i)[I(x_i, y_i) - I_L(\rho, \theta)]^2}{\sum_i C(x_i, y_i)}. \tag{14}$$

Let $I(x_i, y_i)$ be the grayscale image at point (x_i, y_i), and let $I_L(\rho, \theta)$ be the image rendered from the parametric crater model. We use Lambertian shading, which models diffuse reflection, as on Mars diffuse reflection dominates [38]. The intensity of a diffuse point is calculated as the cosine of the angle between the direction to the sun (derived from the HiRISE metadata), L, and the surface normal, N (equivalently, the dot product between the two vectors)

$$I_L(\rho, \theta) = L \cdot N(\rho, \theta). \tag{15}$$

Each surface normal, N, is determined by calculating the surface gradient of the parametric crater model. We use a graphics processing unit to efficiently calculate the surface normals.

E. Priors

From the work of McEwen and Bierhaus [14], we know some prior information about craters: 1) primary craters are generally circular, while low-velocity secondary craters tend to be more elliptical; 2) the semimajor axis of a secondary crater ellipse is aligned with a ray extending from its parent primary crater; 3) secondary crater diameters are typically less than 5% of their primary crater's diameter; and 4) secondary craters are shallower when compared with the primary craters of similar size. We incorporated these differences in shape, diameter, and crater depth into our model by specifying three different sets of prior distributions over r, r_m, and h_s: one for primary craters, one for secondary craters, and a third that assumed uniform priors over r, r_m, and h_s. In all three cases, all other parameters (h_r, ϕ, α, longitude, and latitude) were given uniform priors.

We used normal distributions as the form of the prior over r, r_m, and h_s. For primary craters, the Gaussian means (μ_r, μ_{r_m}, and μ_{h_s}) and the standard deviations (σ_r, σ_{r_m}, and σ_{h_s}) were estimated based on craters with diameters between 1000 and 1350 m from the Robbins and Hynek [22] crater database. For secondary craters, we estimated the means and standard deviations based on empirical measurements of 30 small (50 m < diameter < 350 m) craters observed within DTEED_025459_1895_026514_1895_A01, which are interpreted to be secondary craters from Zunil.

V. Crater Parameter Inference

Given a data source, either a DTM or grayscale image, with the appropriate likelihood function and a prior distribution set (either primary, secondary, or all-uniform), we then computed the posterior distribution according to (1). As the posterior is a nonconvex function and likely to have many local optima, we developed an MCMC sampler to search for the best parameter values. In particular, we used the MH algorithm [39], using a normal distribution as the proposal distribution. According to the MH algorithm, a new proposed set of parameter values is sampled from the proposal distribution centered on the current set of parameter values; this new proposed sample is evaluated against the current parameters and, if accepted, becomes the new parameter set, otherwise another proposed sample is drawn. This process repeats with the MH algorithm acceptance test guaranteeing that after sufficient samples, all future samples are drawn from the true posterior distribution. We select the maximum posterior sample, known as the maximum *a posteriori* (MAP) estimate, as the estimate for the best fit of the crater parameters.

A. Crater Profile Evaluation

Each MAP estimate of model parameters determines a 3-D surface that is hypothesized to estimate a best fit to the evidence (DTM or grayscale image) of the crater. In order to evaluate how well the model fits, we compute a crater profile by averaging 360 2-D profiles generated by slicing the 3-D surface by a perpendicular plane that passes through the center of the crater model, and rotating the plane at 1° intervals. Because craters are not rotationally symmetric, we cannot compute a crater profile by simply averaging all 360 profiles of a given crater; instead, we average the profiles after transforming them to have the same crater rim distance to the center. For each crater, we compare the DTM crater profile to the inferred crater profile to evaluate the quality of the inferred crater model. After computing the crater profiles, several error measures are derived. First, $e_{\text{floor\_}h}$ is the difference between the modeled height of the crater floor and the observed height of the DTM crater profile, measured at the center of each crater. Additionally, $e_{\text{rim\_}x}$ and $e_{\text{rim\_}h}$ are the differences between the x location and the height of the crater rim, respectively, measured between the modeled and observed crater profiles. Finally, e_{SAD} is the sum of absolute height differences between each point from the inferred crater and the DTM crater.

B. Normalization of Parameters and Error Measures

In our set of evaluation craters, primary crater diameters are about twice as large as the secondary crater diameters. Therefore, to facilitate comparisons, we normalized each crater parameter and error measure by scaling the crater by a factor that would make the semimajor axis length equal one. Additionally, the value of e_{SAD} is normalized by the total number of points summed in the error calculation.

C. Results

Tables II and III show the error measures after inferring the parametric crater model using the DTM and grayscale likelihoods, respectively. In each table, each row corresponds to a different crater, where $craters_{1\text{–}3}$ are assumed to be primary and $craters_{4\text{–}6}$ are assumed to be secondary crater types. The two major columns are labeled uniform prior and appropriate prior. Uniform prior indicates the model included the set of priors that are all uniformly distributed, while appropriate prior means the set of priors was used that matches the assumed crater type (e.g., priors for primary craters were used for the assumed primary type). Within each major column, the four subcolumns correspond to the error measures: $e_{\text{floor\_}h}$, $e_{\text{rim\_}x}$, $e_{\text{rim\_}y}$, and e_{SAD}, with mean errors and their standard deviations calculated based on 100 runs of the MH sampler, where each run involves changing the random seed and using different initial parameter values. The final column for each table, labeled d_{SAD}, shows the change in percent difference of the e_{SAD} error measures between the uniform prior and the appropriate prior for each crater.

TABLE II
CRATER MODEL ERRORS, INFERRED USING DTM LIKELIHOOD

Crater	Uniform prior				Appropriate prior				d_{SAD} (%)
	e_{floor_h}	e_{rim_x}	e_{rim_h}	e_{SAD}	e_{floor_h}	e_{rim_x}	e_{rim_h}	e_{SAD}	
$crater_1$	0.00 ± 0.00	0.13 ± 0.01	0.03 ± 0.00	2.60 ± 0.10	0.01 ± 0.00	0.12 ± 0.01	0.03 ± 0.00	2.33 ± 0.09	10.38
$crater_2$	0.01 ± 0.00	0.11 ± 0.07	0.04 ± 0.01	4.67 ± 0.23	0.01 ± 0.00	0.10 ± 0.00	0.04 ± 0.00	4.31 ± 0.05	7.71
$crater_3$	0.01 ± 0.00	0.12 ± 0.13	0.04 ± 0.01	4.65 ± 0.55	0.01 ± 0.00	0.09 ± 0.04	0.04 ± 0.00	4.05 ± 0.20	12.90
$crater_4$	0.00 ± 0.00	0.10 ± 0.01	0.02 ± 0.00	3.81 ± 0.05	0.00 ± 0.00	0.12 ± 0.01	0.02 ± 0.00	4.00 ± 0.04	-4.98
$crater_5$	0.01 ± 0.00	0.14 ± 0.06	0.07 ± 0.01	5.46 ± 0.55	0.01 ± 0.00	0.16 ± 0.02	0.07 ± 0.01	5.31 ± 0.16	2.75
$crater_6$	0.03 ± 0.00	0.22 ± 0.03	0.04 ± 0.01	5.42 ± 0.16	0.02 ± 0.00	0.26 ± 0.03	0.04 ± 0.01	5.53 ± 0.09	-2.03

TABLE III
CRATER MODEL ERRORS, INFERRED USING GRAYSCALE LIKELIHOOD

Crater	Uniform prior				Appropriate prior				d_{SAD} (%)
	e_{floor_h}	e_{rim_x}	e_{rim_h}	e_{SAD}	e_{floor_h}	e_{rim_x}	e_{rim_h}	e_{SAD}	
$crater_1$	0.09 ± 0.00	0.06 ± 0.01	0.08 ± 0.01	4.88 ± 0.23	0.07 ± 0.00	0.02 ± 0.01	0.16 ± 0.01	5.92 ± 0.23	-21.31
$crater_2$	0.14 ± 0.01	0.08 ± 0.01	0.04 ± 0.01	10.27 ± 0.43	0.10 ± 0.00	0.01 ± 0.01	0.05 ± 0.00	8.15 ± 0.20	20.64
$crater_3$	0.19 ± 0.01	0.02 ± 0.00	0.10 ± 0.01	10.08 ± 0.62	0.22 ± 0.00	0.00 ± 0.00	0.10 ± 0.00	11.00 ± 0.17	-9.13
$crater_4$	0.07 ± 0.01	0.04 ± 0.02	0.06 ± 0.01	7.14 ± 0.72	0.04 ± 0.02	0.07 ± 0.15	0.04 ± 0.04	5.51 ± 1.88	22.82
$crater_5$	0.42 ± 0.39	1.10 ± 1.47	0.06 ± 0.14	23.54 ± 52.15	0.09 ± 0.03	0.16 ± 0.04	0.05 ± 0.02	9.23 ± 0.93	60.79
$crater_6$	0.13 ± 0.04	0.09 ± 0.07	0.03 ± 0.01	11.57 ± 1.93	0.06 ± 0.01	0.14 ± 0.04	0.03 ± 0.01	8.93 ± 0.92	22.81

Comparing columns $e_{\text{floor\_}h}$ and $e_{\text{rim\_}h}$ from Table II with Table III, we see a trend that the DTM likelihood outperforms the grayscale likelihood, but when we examine the $e_{\text{rim\_}x}$ error measure, we observe the opposite trend. This indicates that the DTM likelihood does best when fitting the crater center, sediment infill, and rim height but performs poorly in fitting the rim location. This occurs because the DTM likelihood only considers the height of the points and ignores the crater surface normals and their effect on the reflected light. When the surface normal changes in the crater model, the rim region does not exhibit great change in height, but does exhibit an abrupt change in illumination intensity. The grayscale likelihood uses the surface normal information, resulting in a better inference for the crater rim location.

D. Limitations of the Likelihood Models

It can be advantageous to convert intensities (i.e., energies measured by the remote sensing system) to scaled intensities that maximize the contrast (or stretch) within an image. However, clipping can occur when the intensity of a certain pixel falls outside the minimum and the maximum value that can be represented. Clipping is particularly problematic for impact craters that can include deeply shadowed or brightly illuminated faces. For example, $crater_3$, imaged within HiRISE image ESP_037948_1645_RED_C_01_ORTHO, includes sun-facing craters walls that result in clipping, where surface normals approach the orientation of the sun directional vector. $crater_3$ fits are good near the rim and the crater ejecta region, which results in an accurate location for the crater rim ($e_{\text{rim\_}x}$ is almost zero). However, MCMC failed to find an accurate geometry in the center region, and in most cases inferred a deeper crater ($e_{\text{floor\_}h}$ is three times bigger in this crater than in the other craters). This poor fit is interpreted due to clipping in the grayscale image because the crater geometry is correctly inferred using the DTM likelihood. Additionally, $crater_2$, which is south of $crater_3$ in the same image, has a better fit overall using the grayscale likelihood because it was not affected by clipping.

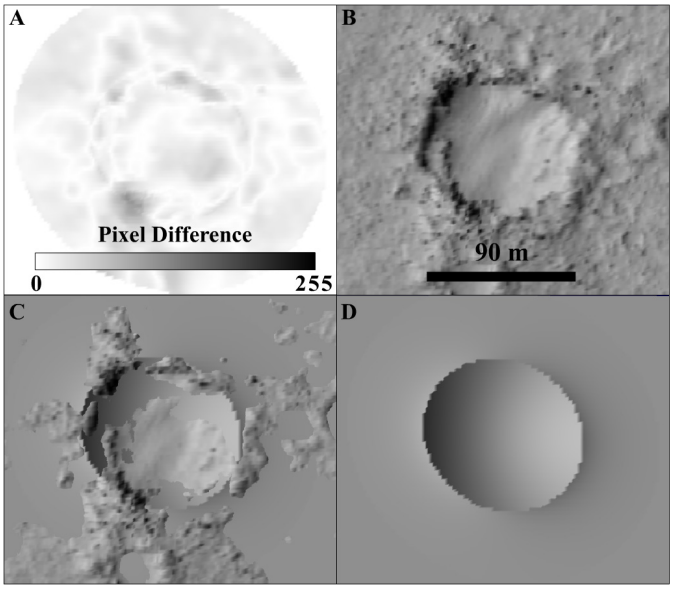

Fig. 2. Analysis of the rendered inferred crater model for $crater_6$ using the grayscale likelihood. (A) Error function between (B) $crater_6$ from HiRISE image ESP_037948_1645_RED_C_01_ORTHO and (D) rendered inferred crater. In (A), black is the maximal pixel difference and white is none. (C) $crater_6$ from DTM DTEED_025459_1895_026514_1895_A01 overlapping with the 3-D geometry of the inferred crater.

The $crater_1$ model was complicated by its crater rim height asymmetry. The appropriate (i.e., primary crater) prior has yielded better results in estimating the center (lower $e_{\text{floor\_}h}$) and rim location (lower $e_{\text{rim\_}x}$) for this crater, but had trouble explaining its irregular rim height, which resulted in a higher $e_{\text{rim\_}h}$ using the appropriate prior, relative to the uniform prior.

Secondary craters, $crater_4$, $crater_5$, and $crater_6$, lie in a region with almost no image clipping, yielding a better fit overall for these craters. Fig. 2 shows a rendering of the inferred crater model for $crater_6$ using the grayscale likelihood. The fit is good, except for the bottom-left segment, where the crater wall casts a shadow that we do not include in our modeling.

E. Influence of Priors

Fitting $crater_5$ was challenging because it partially overlaps with another crater. Using a uniform prior allowed the parameters to vary widely, which resulted in the algorithm attempting to fit landforms within the grayscale image that were not craters. However, using the DTM data, the algorithm resulted in a bimodal parametrization, alternatively fitting one of the two overlapping craters. Consequently, standard deviation for the e_{SAD} value for $crater_5$ MCMC inference is two orders of magnitude higher than for the rest of the fitted craters. Changing to the secondary crater prior for $crater_5$ resulted in an improvement by more reliably finding the location of the crater rim by constraining the search to elliptical craters.

When comparing Table II (DTM input) uniform prior column, $e_{\text{floor\_}h}$, with the appropriate prior column, $e_{\text{floor\_}h}$, we see almost no change in error; however, comparing Table III (grayscale input) uniform prior column, $e_{\text{floor\_}h}$, with the appropriate prior column, $e_{\text{floor\_}h}$, there is a decrease in $e_{\text{floor\_}h}$. Using the DTM likelihood, the error function is sensitive to height differences, and thus the priors based on height values are not as informative, but when using the grayscale likelihood, the error function is more sensitive to changes in surface normals rather than height, resulting on an informative prior, and overall better fit. Our primary crater prior has been extrapolated from characteristics of primary craters of 1000–1350 m diameter, and this extrapolation caused some of our priors to be detrimental to the grayscale crater fit. For instance, going from the uniform prior to the informed prior for $crater_{1\text{–}3}$ resulted in an increase in error for $e_{\text{rim\_}h}$, even though there was a decrease in error for $e_{\text{rim\_}x}$. However, the primary crater prior did not significantly affect the inference when using the DTM likelihood because the likelihood for the DTM focuses on the difference in heights between the inferred and observed crater heights. Therefore, in calculating the posterior probability distribution, which is equal to the prior times the likelihood, the fit was insensitive to the primary crater prior because it was outweighed by the likelihood. The behavior is different for a grayscale likelihood because the error function is sensitive to changes in surface normals, relying on the priors to be informative of the shape of the crater. This resulted in higher overall errors for two out of the three primary craters, relative to the fits obtained using uniform priors, as evidenced by negative d_{SAD} values for craters $crater_1$ and $crater_3$. This is due mainly to an increase in $e_{\text{rim\_}h}$, in turn due to the usage of a poor h_r prior for primary craters. However, usage of the informed prior lead to a reduction in $e_{\text{rim\_}x}$ by improving the crater shape parameter prior, r_m. In contrast, using informed secondary crater priors, error measures increased for rim location, $e_{\text{rim\_}x}$, leading to slightly higher errors when using the DTM likelihood, but substantial improvements to all error measures when fitting the grayscale likelihood. This suggests that the r_m prior is poor, but the priors for h_r and h_s are highly informative.

VI. Crater Parameters Projection

The parametric crater model involves a number of parameters, which can be grouped to form a high-dimensional crater parameter vector. The t-SNE [26] is a nonlinear dimensionality reduction technique that reduces high-dimensional data into a lower dimensional space and is often used to project data to two dimensions to facilitate visualization. In t-SNE, similar vectors are modeled by nearby points in the lower dimensional projection. t-SNE constructs a probability distribution [defined in (16)] over pairs of high-dimensional vectors, in our case the crater model parameters. The more similar vectors are, the higher the probability of being chosen to be embedded as a neighbor, while dissimilar vectors have smaller probability. Next, t-SNE defines a similar probability distribution [defined in (17)] over the points in the 2-D embedding map by minimizing the Kullback–Leibler divergence [40], which measures how one probability distribution diverges from another. We define X_i as the high-dimensional crater parameter vector that describes the crater geometry. Maaten and Hinton [26] state that the similarity of data point X_i to data point X_j is the conditional probability, $p_{j|i}$, that X_i would pick X_j as its neighbor, if they were picked in proportion to their Gaussian probability density having mean X_i. $p_{j|i}$ is computed by

$$p_{i|j} = \frac{e^{\frac{-\|X_i - X_j\|}{2\sigma_i^2}}}{\sum_{k \neq i} e^{\frac{-\|X_i - X_k\|}{2\sigma_i^2}}}. \tag{16}$$

We use the Maaten and Hinton [26] method to calculate σ_i, in which smaller values of σ_i are used in denser parts of the data space. They also define $q_{i|j}$ as the similarity measure between two points, $\hat{X}_i$ and $\hat{X}_j$, in the projected 2-D space

$$q_{i|j} = \frac{(1 + \|\hat{X}_i - \hat{X}_j\|^2)^{-1}}{\sum_{k \neq i}(\|\hat{X}_i - \hat{X}_k\|^2)^{-1}}. \tag{17}$$

The algorithm then proceeds to minimize the Kullback–Leibler divergence between both distributions, $p_{i|j}$ and $q_{i|j}$.

The t-SNE transformation does not transform the data to physical units. Instead, it is represented by abstract units defined by a probability measure. The physical interpretation for two crater parameter vectors that are similar is that their Euclidean distance is small. For example, after parameter normalization, two craters that have similar h_s, r_m, and h_r would be close to one another, while if any of these parameters is widely different, the Euclidean distance between the crater parameter vectors would be large.

We normalize all crater parameters as explained in Section V-B. Fig. 3 shows six plots of t-SNE embedding of inferred crater parameter vectors. Within each plot, each row uses a different prior: uniform, primary, and secondary crater priors. Each column uses a different likelihood: DTM and grayscale likelihood. Each data point is a 2D t-SNE projection of the inferred crater parameter vector, and parameterizations are inferred 100 times for each crater, resulting in each plot containing 600 data points for all six craters.

As mentioned in Section V-C, $crater_5$ partially overlaps another crater. Using the DTM likelihood with a uniform prior resulted in $crater_5$ parameters forming two clusters, which each clustering corresponds to the properties of one of the two overlapping craters. In contrast, when applying a grayscale likelihood with a uniform prior to $crater_5$, 63 of 100 parameterizations cluster near the other secondary craters, $crater_6$

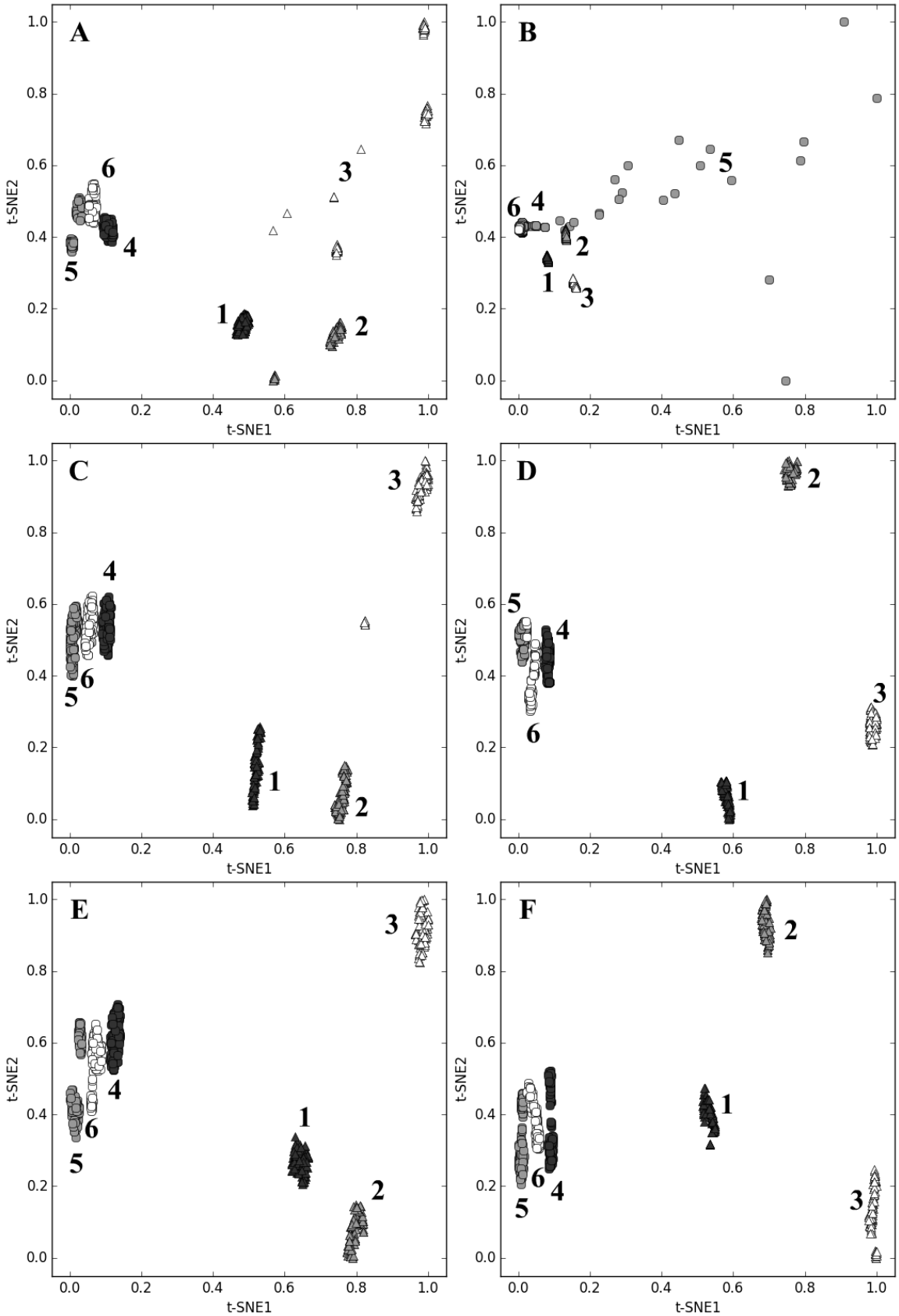

Fig. 3. t-SNE embedding of crater parameters, where each data point is a 2-D projection of the crater parameter vector, and each plot contains 100 inferred vectors for each of six craters. (A), (C), and (E) DTM likelihood. (B), (D), and (F) Grayscale likelihood. (A) and (B) Uniform prior. (C) and (D) Primary crater prior. (E) and (F) Secondary crater prior. Within each plot, each cluster has a number indicating the crater it was inferred from. Triangle: craters interpreted as primary. Circles: craters interpreted as secondary. Numbers that correspond to the crater names are shown in Table I.

and $crater_4$. The remaining points are spread out, as shown in Fig. 3. This suggests that some of the parameters inferred for $crater_5$ are widely different and the algorithm may be attempting to parameterize some landforms that are not impact craters. Using a primary or secondary prior causes $crater_5$ to be restricted to geometries that resemble secondary craters, guiding the parameter search to fit the crater.

In our crater model, the rim height is assumed to be constant for all values of θ. When fitting craters using a uniform prior and a DTM likelihood, the irregular heights of rim of $crater_3$ resulted in some MCMC runs inferring different parameters for the crater rim geometry, leading to some parameterizations to diverge into separate clusters. Using a primary or secondary crater prior caused the parametrization between craters to be consistent, eliminating the cluster divergence. Additionally, this does not seem to pose an issue for the grayscale likelihood, and we attribute the better performance of the algorithm in this case to the continuous visual appearance of the rim due to a smoother change in the orientation of the surface normal.

In general, t-SNE assigns each primary crater (i.e., $craters_{1–3}$) to a widely separable clusters, whereas the secondary craters (i.e., $craters_{4–6}$) concentrate within a single cluster. We interpret this to represent differences in the morphologies of the three primary craters, which formed at different times and have experienced different modification histories, whereas all three secondary craters are of similar size, would have formed at the same time, and have undergone similar postemplacement modification, which resulted in similar crater geometries and parameterizations.

VII. Conclusion

Subkilometer craters, interpreted as secondary craters, share common features that allow their inferred crater parameters to cluster together under the t-SNE projection. Primary and secondary craters are also separable within the t-SNE projection using either a DTM or grayscale likelihood. Informed priors did not consistently improve crater fits for both primary and secondary craters, but they substantially reduce the variability in the parameterized fits of both crater types, thereby improving their separability using t-SNE.

Our model can be improved in a number of ways: 1) empirically measuring the geometry of a large number of subkilometer-scale primary craters to inform the primary priors, rather than extrapolating priors from the characteristics of 1000–1350-m-diameter craters within the Robbins and Hynek [22] database; 2) using a larger number of secondary craters to improve secondary priors; and 3) modifying the parameterization of crater rim heights for both primary and secondary craters to vary with θ to better represent the irregular shapes of impact crater rims. While our model can be improved with better informed priors, our results here support our proposal that the Bayesian framework provides a useful method to model and differentiate primary and secondary craters, making it feasible to accurately date newer surfaces on Mars, where only small (<1 km diameter) impact craters are available.

References

[1] W. K. Hartmann, "Martian cratering 8: Isochron refinement and the chronology of Mars," *Icarus*, vol. 174, no. 2, pp. 294–320, Apr. 2005.

[2] S. T. Stewart and G. J. Valiant, "Martian subsurface properties and crater formation processes inferred from fresh impact crater geometries," *Meteoritics Planetary Sci.*, vol. 41, no. 10, pp. 1509–1537, Oct. 2006.

[3] A. M. Bramson *et al.*, "Widespread excess ice in Arcadia Planitia, Mars," *Geophys. Res. Lett.*, vol. 42, no. 16, pp. 6566–6574, Aug. 2015.

[4] A. J. Brown, S. Byrne, L. L. Tornabene, and T. Roush, "Louth crater: Evolution of a layered water ice mound," *Icarus*, vol. 196, no. 2, pp. 433–445, Aug. 2008.

[5] C. M. Dundas, L. P. Keszthelyi, V. J. Bray, and A. S. McEwen, "Role of material properties in the cratering record of young platy-ridged lava on Mars," *Geophys. Res. Lett.*, vol. 37, no. 12, L12203, Jun. 2010. [Online]. Available: https://agupubs.onlinelibrary.wiley.com/doi/full/10.1029/2010GL042869, doi: 10.1029/2010GL042869.

[6] M. P. Golombek *et al.*, "Small crater modification on Meridiani Planum and implications for erosion rates and climate change on Mars," *J. Geophys. Res., Planets*, vol. 119, no. 12, pp. 2522–2547, Dec. 2014.

[7] M. E. Landis, S. Byrne, I. J. Daubar, K. E. Herkenhoff, and C. M. Dundas, "A revised surface age for the North Polar Layered Deposits of Mars," *Geophys. Res. Lett.*, vol. 43, no. 7, pp. 3060–3068, Apr. 2016.

[8] R. Arvidson *et al.*, "Standard techniques for presentation and analysis of crater size-frequency data," *Icarus*, vol. 37, no. 2, pp. 467–474, Feb. 1979.

[9] R. G. Strom, R. Malhotra, T. Ito, F. Yoshida, and D. A. Kring, "The origin of planetary impactors in the inner solar system," *Science*, vol. 309, no. 5742, pp. 1847–1850, Sep. 2005.

[10] B. A. Ivanov, "Mars/Moon cratering rate ratio estimates," *Space Sci.*, vol. 96, nos. 1–4, pp. 87–104, Apr. 2001.

[11] I. Daubar, A. S. McEwen, S. Byrne, M. R. Kennedy, and B. Ivanov, "The current martian cratering rate," *Icarus*, vol. 225, no. 1, pp. 506–516, Jul. 2013.

[12] S. C. Werner, B. A. Ivanov, and G. Neukum, "Theoretical analysis of secondary cratering on Mars and an image-based study on the Cerberus Plains," *Icarus*, vol. 200, no. 2, pp. 406–417, Apr. 2009.

[13] A. S. McEwen *et al.*, "The rayed crater Zunil and interpretations of small impact craters on Mars," *Icarus*, vol. 176, no. 2, pp. 351–381, Aug. 2005.

[14] A. S. McEwen and E. B. Bierhaus, "The importance of secondary cratering to age constraints on planetary surfaces," *Annu. Rev. Earth Planetary Sci.*, vol. 34, pp. 535–567, May 2006.

[15] H. Jahn, "Crater detection by linear filters representing the Hough transform," *Proc. SPIE*, vol. 2357, p. 427, Aug. 1994.

[16] J. R. Kim, J. P. Muller, S. van Gasselt, J. G. Morley, and G. Neukum, "Automated crater detection, a new tool for Mars cartography and chronology," *Photogramm. Eng. Rem. Sens.*, vol. 71, no. 10, pp. 1205–1217, Oct. 2005.

[17] E. R. Urbach and T. F. Stepinski, "Automatic detection of sub-km craters in high resolution planetary images," *Planet Space Sci.*, vol. 57, no. 7, pp. 880–887, 2009.

[18] L. Bandeira, J. Saraiva, and P. Pina, "Impact crater recognition on Mars based on a probability volume created by template matching," *IEEE Trans. Geosci. Remote Sens.*, vol. 45, no. 12, pp. 4008–4015, Dec. 2007.

[19] L. Bandeira, W. Ding, and T. F. Stepinski, "Detection of sub-kilometer craters in high resolution planetary images using shape and texture features," *Adv. Space Res.*, vol. 49, no. 1, pp. 64–74, Jan. 2012.

[20] Y. Wang, W. Ding, K. Yu, H. Wang, and X. Wu, "Crater detection using Bayesian classifiers and LASSO," in *Proc. IEEE Conf. Anthol.*, Jan. 2013, pp. 1–5.

[21] J. P. Cohen, H. Z. Lo, T. Lu, and W. Ding. (2016). "Crater detection via convolutional neural networks." [Online]. Available: https://arxiv.org/abs/1601.00978

[22] S. J. Robbins and B. M. Hynek, "A new global database of Mars impact craters ≥1 km: 1. Database creation, properties, and parameters," *J. Geophys. Res., Planets*, vol. 117, no. E5, E05004, May 2012. [Online]. Available: https://agupubs.onlinelibrary.wiley.com/doi/abs/10.1029/2011JE003966, doi: 10.1029/2011JE003966.

[23] H.-J. Hsu and N. G. Barlow, "Investigation of the relationship of crater depths and diameters in selected regions of Mars," in *Proc. 44th Lunar Planetary Sci. Conf.*, vol. 11. 2013, pp. 1–2.

[24] A. S. McEwen *et al.*, "Mars reconnaissance orbiter's high resolution imaging science experiment (HiRISE)," *J. Geophys. Res., Planets*, vol. 112, no. E5, pp. 1204–1227, 2007.

[25] R. L. Kirk *et al.*, "Ultrahigh resolution topographic mapping of Mars with MRO HiRISE stereo images: Meter-scale slopes of candidate Phoenix landing sites," *J. Geophys. Res., Planets*, vol. 113, no. E3, pp. 1347–1350, Mar. 2008.
[26] L. van der Maaten and G. Hinton, "Visualizing data using t-SNE," *J. Mach. Learn. Res.*, vol. 9, pp. 2579–2605, Nov. 2008.
[27] T. Atherton and D. J. Kerbyson, "Size invariant circle detection," *Image Vis. Comput.*, vol. 17, no. 11, pp. 795–803, Sep. 1999.
[28] Y. Cheng, A. E. Johnson, L. H. Matthies, and C. F. Olson, "Optical landmark detection for spacecraft navigation," *Adv. Astron. Sci.*, vol. 114, no. 3, pp. 1785–1803, 2003.
[29] T. Barata, E. I. Alves, J. Saraiva, and P. Pina, "Automatic recognition of impact craters on the surface of Mars," in *Proc. Int. Conf. Image Anal. Recognit.*, 2004, pp. 489–496.
[30] R. C. Gonzalez and R. E. Woods, "Morphological image processing," in *Digital Image Processing*, vol. 2. New York, NY, USA: Prentice-Hall, 2002, pp. 520–550.
[31] M. L. Comer and E. J. Delp, "Morphological operations for color image processing," *Electron. Imag.*, vol. 8, no. 3, pp. 279–290, 1999.
[32] G. Salamunićcar and S. Lončarić, "Method for crater detection from martian digital topography data using gradient value/orientation, morphometry, vote analysis, slip tuning, and calibration," *IEEE Trans. Geosci. Remote Sens.*, vol. 48, no. 5, pp. 2317–2329, May 2010.
[33] R. Martins, P. Pina, J. S. Marques, M. Silveira, and M. Silveira, "Crater detection by a boosting approach," *IEEE Geosci. Remote Sens. Lett.*, vol. 6, no. 1, pp. 127–131, Jan. 2009.
[34] W. Ding *et al.*, "Subkilometer crater discovery with boosting and transfer learning," *ACM Trans. Intell. Syst. Technol.*, vol. 2, no. 4, pp. 1–22, Jul. 2011.
[35] Y. Wang, G. Yang, and L. Guo, "A novel sparse boosting method for crater detection in the high resolution planetary image," *Adv. Space Res.*, vol. 56, no. 5, pp. 982–991, Sep. 2015.
[36] H. J. Melosh, *Impact Cratering: A Geologic Process* (Oxford Monographs on Geology and Geophysics), vol. 11. London, U.K.: Oxford Univ. Press, 1989, p. 253.
[37] *Removing Linear Trends*. Accessed: Apr. 3, 2017. [Online]. Available: https://www.mathworks.com/help/matlab/ref/detrend.html
[38] A. Shaw, M. J. Wolff, F. P. Seelos, S. M. Wiseman, and S. Cull, "Surface scattering properties at the Opportunity Mars rover's traverse region measured by CRISM," *J. Geophys. Res., Planets*, vol. 118, no. 8, pp. 1699–1717, Aug. 2013.
[39] S. Chib and E. Greenberg, "Understanding the Metropolis-Hastings algorithm," *Amer. Stat.*, vol. 49, no. 4, pp. 327–335, 1995.
[40] S. Kullback and R. A. Leibler, "On information and sufficiency," *Ann. Math. Stat.*, vol. 22, no. 1, pp. 79–86, Mar. 1951.

Rodrigo Savage was born in Mexico City, Mexico, in 1989. He received the B.E. degree in computer engineering from Mexico National Autonomous University, Mexico City. He is currently pursuing the Ph.D. degree with the Department of Electrical and Computer Engineering, The University of Arizona, Tucson, AZ, USA.

Since then, he has been passionate on researching planetary science using machine leaning tools. His research interests include machine learning, planetary science, robotics, and virtual reality.

Leon F. Palafox was born in Mexico City, Mexico, in 1981. He received the B.E. degree in electrical engineering from Mexico National Autonomous University, Mexico City, in 2005, and the M.Sc. and Ph.D. degrees in electrical engineering from The University of Tokyo, Tokyo, Japan, in 2010 and 2013, respectively.

In 2013, he joined the Department of Radiology, University of California at Los Angeles, Los Angeles, CA, USA, as a Post-Doctoral Fellow. In 2014, he became a Post-Doctoral Fellow and in 2015, an Associate Staff Scientist with the Lunar and Planetary Laboratory, The University of Arizona, Tucson, AZ, USA. In 2017, he became a Lecturer with Panamerican University, Mexico City. His research interests include machine learning, molecular biology, neuroscience, planetary science, and astrophysics.

Clayton T. Morrison received the Ph.D. degree in philosophy with specialization in computational cognitive modeling from Binghamton University, Binghamton, NY, USA, in 1998, and the M.Sc. degree in computer science from the University of Massachusetts, Amherst, MA, USA, in 2004.

He spent five years at the University of Southern California Information Sciences Institute, Marina del Rey, CA, USA, for two years as a Director of the Central Intelligence Post-Doctoral Fellowship Program, and then as a Research Computer Scientist. He joined The University of Arizona, Tucson, AZ, USA, in 2008, where he is currently an Associate Professor with the School of Information and a Faculty Member of the Statistics Graduate Interdisciplinary Program. He leads the Machine Learning for Artificial Intelligence Laboratory. His research interests include developing machine learning and statistical modeling approaches to learning structured representations from unstructured, semistructured, and time series data. Applications include natural language processing and machine reading, biological structure and processes, computational music analysis, and modeling the relationships between human facial expressions and decision making. His work has been funded by multiple grants from the National Science Foundation, the Defense Advanced Research Projects Agency, the Air Force Office of Scientific Research, and the Office of Naval Research.

Jeffrey J. Rodriguez (SM'02) received the B.S. degree from The University of Texas at Austin, Austin, TX, USA, in 1984, the M.S. degree from the Massachusetts Institute of Technology, Cambridge, MA, USA, in 1986, and the Ph.D. degree from The University of Texas at Austin in 1990, all in electrical engineering.

Since 1990, he has been a Faculty Member with the Department of Electrical and Computer Engineering, The University of Arizona, Tucson, AZ, USA, where he is the Director of the Signal and Image Laboratory. His research interests include signal/image/video processing and analysis with a particular emphasis on automated image analysis.

Dr. Rodriguez served as the General Chair of the 2016 IEEE Southwest Symposium on Image Analysis and Interpretation and the 2007 IEEE International Conference on Image Processing, and has served on the organizing committees for numerous other technical conferences. From 2005 to 2011, he served on the IEEE Signal Processing Society, Technical Committee on Image, Video, and Multidimensional Signal Processing. From 2003 to 2008, he was the Co-Director of Connection One, Singapore, a National Science Foundation Research Center. From 1996 to 2000, he was an Associate Editor of the IEEE TRANSACTIONS ON IMAGE PROCESSING.

Kobus Barnard (M'03) received the Ph.D. degree in computer science with specialization in computational color constancy from Simon Fraser University, Burnaby, BC, Canada, in 2000.

He then spent two years at the University of California at Berkeley, Berkeley, CA, USA, as a Post-Doctoral Researcher, involved in modeling the joint statistics of images and associated text. He is currently a Professor with the Department of Computer Science, The University of Arizona, Tucson, AZ, USA. He also has appointments in Statistics, Cognitive Science, Electrical and Computer Engineering, and the BIO5 Institute. He leads the Interdisciplinary Visual Intelligence Laboratory. His research interests include interdisciplinary computational intelligence by developing top-down statistical models that are predictive, semantic, and explanatory. Application domains include computer vision, multimedia data, biological structure and processes, astronomy, and human social interaction. His work has been funded by multiple grants from the National Science Foundation, including a CAREER Award, and awards from the Defense Advanced Research Projects Agency, the Office of Naval Research, the Arizona Biomedical Commission, and the University of Arizona BIO5 Institute.

Dr. Barnard received the Governor General Gold Medal across all disciplines for his Ph.D. dissertation.

Shane Byrne was born in Drogheada, Ireland, in 1975. He received the M.Phys. degree in astrophysics from the University of Wales, Cardiff, U.K., in 1998, and the Ph.D. degree in planetary sciences from the California Institute of Technology, Pasadena, CA, USA, in 2003.

After post-doctoral studies at the Massachusetts Institute of Technology, Cambridge, MA, USA, and the U.S. Geological Survey, Flagstaff, AZ, USA, he joined the faculty of the Lunar and Planetary Laboratory, The University of Arizona, Tucson, AZ, USA, in 2007. He specializes in surface processes on planetary bodies especially those that affect, or are driven by, planetary ices. He and his research group have over 80 publications covering the Solar System objects ranging from Mercury to Umbriel. He is involved in the ongoing spacecraft investigations, including HiRISE and CaSSIS imaging for Mars, and Dawn at Ceres. He is also the Director of the Space Imagery Center and a NASA Regional Planetary Image Facility that archives planetary spacecraft and telescopic data not available online and conducts many outreach events.

Christopher W. Hamilton was born in Halifax, Canada, in 1979. He received the B.Sc. degree in earth sciences from Dalhousie University, Halifax, NS, Canada, in 2004, and the Ph.D. degree from the University of Hawaii, Honolulu, HI, USA, in 2010.

After completing his post-doctoral studies at the NASA Goddard Space Flight Center, Greenbelt, MD, USA, he joined the faculty of the Lunar and Planetary Laboratory, The University of Arizona, Tucson, AZ, USA, in 2014. He has 30 publications relating to the study of the Earth, Moon, Mars, and Jupiter's satellite Io, using methods that combine field-based research with remote sensing, machine learning, geoinformatics, and numerical modeling. His research interests include the study of geological surface processes, and, in particular, planetary volcanism and impact cratering on terrestrial planets and moons.